

See discussions, stats, and author profiles for this publication at: <https://www.researchgate.net/publication/263949578>

Interslit Coupling via Ultrafast Dynamics across Gold-Film Hole Arrays

ARTICLE in THE JOURNAL OF PHYSICAL CHEMISTRY C · MAY 2014

Impact Factor: 4.77 · DOI: 10.1021/jp503613t

CITATIONS

2

READS

35

10 AUTHORS, INCLUDING:



Itai Carmeli

Tel Aviv University

37 PUBLICATIONS 744 CITATIONS

SEE PROFILE



Reinhard Schneider

Karlsruhe Institute of Technology

112 PUBLICATIONS 1,126 CITATIONS

SEE PROFILE



Tsofar Maniv

Technion - Israel Institute of Technology

128 PUBLICATIONS 1,507 CITATIONS

SEE PROFILE



Shachar Richter

Tel Aviv University

56 PUBLICATIONS 568 CITATIONS

SEE PROFILE

Interslit Coupling via Ultrafast Dynamics across Gold-Film Hole Arrays

Roman Walther,^{†,●} Itai Carmeli,^{*,‡,●} Reinhard Schneider,[†] Dagmar Gerthsen,^{†,§} Kurt Busch,^{||,⊥} Christian Matyssek,^{||} Ayala Shvarzman,[‡] Tsofar Maniv,[#] Shachar Richter,[‡] and Hagai Cohen^{*,▼}

[†]Laboratory for Electron Microscopy, Karlsruhe Institute of Technology (KIT), D-76128 Karlsruhe, Germany

[‡]Department of Materials Science and Engineering, Faculty of Engineering & University Center for Nano Science and Nanotechnology, Tel-Aviv University, Tel Aviv, 69978, Israel

[§]Center for Functional Nanostructures, Karlsruhe Institute of Technology (KIT), D-76128 Karlsruhe, Germany

^{||}Institut für Physik, AG Theoretische Optik & Photonik, Humboldt-Universität zu Berlin, 12489 Berlin, Germany

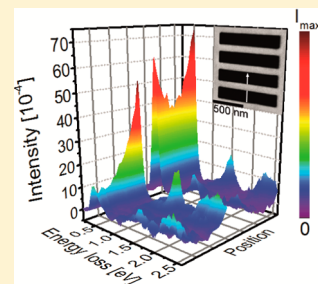
[⊥]Max-Born-Institut, 12489 Berlin, Germany

[#]Schulich Faculty of Chemistry, Technion – Israel Institute of Technology, Haifa 32000, Israel

[▼]Department of Chemical Research Support, Weizmann Institute of Science, Rehovot 76100, Israel

S Supporting Information

ABSTRACT: One-dimensional arrays of submicrometer rectangular holes in 200 nm thin gold films are investigated using electron energy loss spectroscopy combined with scanning transmission electron microscopy (STEM-EELS). Improved energy resolution, down to 0.11 eV, is accomplished in our monochromated transmission electron microscope, allowing the reliable quantification of signals at loss energies as small as 0.43 eV. The standing-wave resonances of individual holes are thus investigated at nanometer-scale spatial resolution, focusing in particular on the effect of neighboring holes. We show how the coupling between holes is facilitated by surface plasmon polaritons (SPPs) propagating on the top and bottom surfaces of the separating metal-film strips. Thus, complex spatiotemporal coupling dynamics emerges, characterized by strong interslit interactions and a phase that can be controlled by varying the width of the metal strip between adjacent holes. Applying real-space real-time numerical simulations and exploiting the short interaction time of 300 keV electrons with the thin gold film, we reveal intriguing features of these ultrafast coupling mechanisms, including unusual line-narrowing and marked SPP signal enhancements in the corresponding EEL spectra. Complementary aspects of the far-field and near-field components in the SPP eigenstates are further demonstrated. Our combined analysis effectively equips STEM-EELS with an excellent temporal resolution and further yields a consistent description of the entangled femtosecond-scale SPP dynamics.



INTRODUCTION

The discovery of extraordinary optical transmission (EOT) through structured thin metal films¹ has drawn attention to the role of light-induced activity at and within the film itself.^{2–6} In particular, EOT involves efficient coupling of the illuminating light-beam to surface-plasmon-polariton (SPP) modes propagating on the metal. This light–SPP coupling is greatly enhanced by introducing holes and sharp edges,⁷ so that even a single hole can exhibit EOT. However, it is widely accepted that momentum transfer processes associated with periodic arrays of holes promise improved light–SPP coupling. Hence, the range and nature of interactions between resonances that are localized in different slits is of considerable interest, notably in view of the dominant role played by short-range interactions in parts of the current EOT literature.^{8,9}

Attempts to optically map the electromagnetic (EM) field structure above and around holes in metallic films^{10–13} generally encounter the problem of limited spatial resolution. A complementary approach, using electron energy loss

spectroscopy (EELS) combined with scanning transmission electron microscopy (STEM), has been recently applied to study with subnanometer lateral resolution the near-field coupling between metallic nanoparticles,^{14,15} as well as the hybridization between SPPs and vacuum-supported waveguide (WG) resonances in isolated holes in free-standing gold films.¹⁶ The focused electron beam provides effective coupling to both far-field (FF) and near-field (NF) EM components,^{17,18} and in contrast to energy-filtered TEM (EFTEM) images,^{19,20} it represents a fast-moving point-like antenna probe with unique features as compared to all broad-beam illumination techniques. In this work, STEM-EELS is exploited for the investigation of local field enhancements in one-dimensional (1D) arrays of rectangular holes with submicrometer size. These STEM-EELS measurements are complemented by real-space real-time

Received: April 13, 2014

Revised: April 27, 2014

Published: April 29, 2014

computations based on the Discontinuous Galerkin Time-Domain (DGTD) approach.^{21,22} Notably, a consistent physical picture emerges that highlights a striking effect regarding the mechanisms of subwavelength nearest-neighbor interactions between adjacent slits. Our combined study further constitutes a unique probe of the transient signal propagation across nanostructured plasmonic systems.

■ EXPERIMENTAL METHODS AND CALCULATION DETAILS

STEM-EELS experiments were performed in an FEI TITAN³ 80–300 transmission electron microscope operated at 300 keV electron energy. The instrument is equipped with a Wien-filter-type electron monochromator and a Gatan Imaging Energy-Filter (GIF) Tridiem model 865 HR. Under monochromatic source conditions, a probe size of about 1 nm is realized in the STEM mode, and for an exposure time of 10 ms, the energy resolution is 0.12 eV. To obtain high-quality data, 50 EEL spectra were acquired at each measurement position with the binned-gain averaging method.²³ This method employs full on-chip binning in the nondispersive direction to speed up the read-out time. As the high binning saturates the charge-coupled device (CCD) camera by the high intensity of the zero-loss peak, the exposure time was reduced to 1 ms, leading also to a slight improvement in energy resolution, about 0.11 eV, due to the reduced effect of stray fields. Additionally, after each measurement, the spectrum was shifted randomly on the CCD camera along the energy-dispersive direction, to effectively average the gain variation of individual pixels, which further improves the signal-to-noise ratio. All spectra except for Figure 2c were acquired with this technique. Alternatively, automated EELS line-scans were performed under control of the TEM imaging and analysis (TIA) software where spectra were taken in step distances of 10 nm with an exposure time of 50 ms. Line scans were repeated 15 times at the same position and averaged to improve the signal-to-noise ratio. Prior to further data analysis, spectra were normalized to the height of the zero-loss peak.

For the data processing, the Richardson–Lucy (RL) algorithm adapted for EELS^{24,25} was applied with a self-written script in Digital Micrograph (Gatan), following the implementation of Al-Bakkar et al.²⁶ This algorithm sharpens the spectra by deconvolving the point-spread function of the spectrometer iteratively. As this function is not known, a vacuum reference spectrum (without a specimen inserted) was used as the point-spread function. A more detailed description of the application of the RL algorithm will be published elsewhere. Seven iterations were used for the spectra as a compromise between sharpening and noise amplification. To evaluate peak intensities, background subtraction was performed by fitting a smooth biexponential function to the right-hand-side tail of the zero-loss peak. All intensities presented here were normalized with respect to the height of the zero-loss peak prior to the application of the RL algorithm.

All samples discussed here contain rectangular holes (slits) in a 200 nm Au film. The thin Au film was prepared by evaporating Au onto a NaCl substrate, which was subsequently floated off and placed on a standard Au TEM grid. Focused-ion-beam milling in an FEI Dual-Beam STRATA 400S was applied to define slits with a length $L = 900$ nm and width $w = 180$ nm. The slits are arranged into 1D arrays with interslit separation distances (the metal bar widths (d) of 100, 270, and 720 nm). As a reference, an isolated slit with the same

dimensions was measured, representing $d \rightarrow \infty$. Prior to insertion into the microscope, each specimen was cleaned in air plasma for 3 min.

Numerical simulations were carried out using the Discontinuous Galerkin Time Domain (DGTD) method²² with the extensions that are necessary to perform EELS simulations as described in ref 21. The only difference is that we use a pure scattered field formalism here, which gives direct access to the field induced by the electron. The permittivity of the gold film is approximated by a single Drude and three Lorentz terms, which give a reasonable approximation to the data measured by Johnson and Christy²⁷ over the entire energy range.

The gold film was made finite with a size of at least $3 \times 3 \mu\text{m}^2$ to reduce artifacts from the edges. Except for a small feature around 0.4 eV (cf. Figure 2b), which, however, is well below the fundamental resonance, the spectrum is entirely free of artifacts. The film was surrounded by air and perfectly matched layers to reduce reflections from the boundary of the computational domain. Third-order elements were used with element sizes down to 10 nm to accurately resolve the incident field of the electron. The simulated spectra were convoluted with a Gaussian function of 100 meV full-width at half-maximum, accounting for the finite experimental energy resolution and the corresponding spectral broadening.

■ RESULTS AND DISCUSSION

Figure 1a presents a series of EEL spectra along a line-scan across two slits of a four-slit array. The scan direction is indicated by an arrow in the high-angle annular dark-field (HAADF) STEM image (Figure 1b). Below the Au surface plasmon at 2.4 eV, cavity resonances of the $L = 900$ nm slit length are well observed at energy losses of ≈ 0.5 and ≈ 1.5 eV. EELS detection of similar resonances was already reported,¹⁶

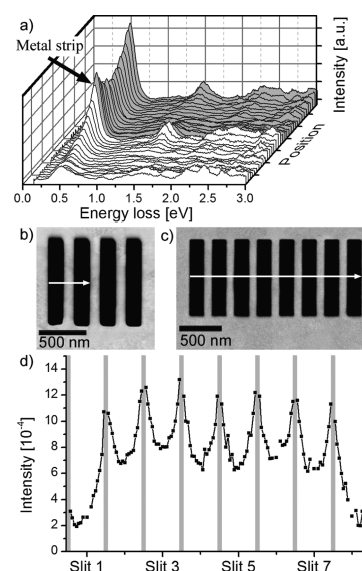


Figure 1. (a) EEL spectra taken along a line-scan across half of a four-slit system, skipping over the metal strip as indicated. Inner slit spectra are marked in gray. (b,c) HAADF images of a four-slit array and an eight-slit array, respectively. Arrows show the scan directions. (d) An intensity profile (area under the peak) of the fundamental cavity mode in an eight-slit array, taken along the line indicated in (c). All spectra shown were treated with seven iterations of the RL algorithm followed by a biexponential background subtraction. In both arrays, the metal bars that separate the slits are $d = 100$ nm wide.

enabled by the breakdown of momentum conservation and the appearance of scattering channels with momentum transfer different from ω/ν , where ω is the SPP frequency and ν is the beam-electron velocity. Notably, the fundamental line at $\omega_1 \approx 0.5$ eV (a value that slightly varies with both electron beam position and array parameters, not shown) is considerably red-shifted relative to the bare EM standing wave (the 1800 nm wavelength) within the slit.^{4,7}

Further, Figure 1a exhibits pronounced near-field (NF) characteristics, manifested by sharply decaying tails,¹⁶ yet the signal strength at the outermost slit wall is drastically weaker than at its immediate neighboring edge, and in the inner slits, an additional signal increase is seen. A similar behavior is presented in Figure 1d by the integrated intensity of the fundamental line, ω_1 , across an eight-slit array (see the corresponding HAADF STEM image in Figure 1c): it rises strongly from the outer to the adjacent inner slits, while showing only small variations between the inner slits. In a complementary set of samples, line intensity enhancements of ω_1 across the very first slit in the array were evaluated for different numbers N of slits (not shown). These enhancements exhibited a striking change when a second slit was introduced, while upon introducing additional slits, this dependence on N quickly saturated (see SI for details).

The above results indicate the emergence of strong, short-range interslit interactions that far exceed the corresponding intraslit edge-to-edge coupling strengths. It is attributed to mediating SPPs that propagate on the top (SPP^{top}) and bottom (SPP^{bot}) faces of the metal strip connecting neighboring slits. These top and bottom SPPs interact effectively with SPPs of the slit walls (SPP^{wall}) across common slit edges. To better understand the coupling mechanisms, we focus the discussion on the relatively simple case of two slits only, noting that the probe is entirely confined to a specific slit (the excited slit), such that the influence of and the effect on a neighboring slit can be neatly inspected.

Figure 2a shows selected spectra along the inner wall (at $L/2$, $L/4$, $L/8$, $L/16$, and $L/32$) of a two-slit system, all recorded at 20 nm distance from the wall. The width of the central metal strip is $d = 100$ nm. Besides the Au surface plasmon at $\omega_s \approx 2.4$ eV and the fundamental cavity mode, ω_1 , the second, third, and

even the fourth harmonic, denoted by ω_2 , ω_3 , and ω_4 , are clearly resolved. Numerically calculated spectra for the same system dimensions are displayed in Figure 2b. Except for a low-energy artifact shoulder around 0.4 eV (originating from the limited film size in the lateral plane), both major intensity variations and line-shifts are well reproduced. The color-coded line-scan along the long axis in Figure 2c demonstrates spatial intensity variations of the ω_n multiples that roughly match ideal cavity modes: ω_2 vanishes at the center, $L/2$, and reaches maximum intensity at $L/4$; ω_3 exhibits reduced intensity at $L/4$; and ω_4 vanishes at both positions. Note that the ω_n values in Figure 2a,b obey an almost linear dependence, as expected from the light-line branch of SPPs.⁷ On the other hand, none of these multiples tend to vanish toward the slit corner, as might be naively expected from an ideal cavity mode.

A scan perpendicular to the long axis at $L/2$ further highlights the peak enhancements and line-shifts across the slit: Two representative spectra are shown in Figure 3a (measured)

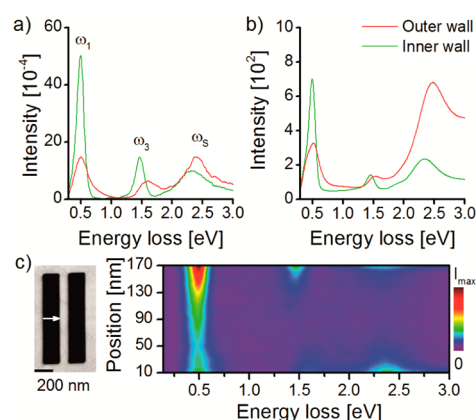


Figure 3. (a) Experimental and (b) simulated EEL spectra taken at 10 nm distance from the outer (light green) and inner (red) walls in a two-slit system with $d = 100$ nm. (c) HAADF STEM image and EELS line-scan along the short slit axis (cf. white arrow).

and in Figure 3b (simulated), at 10 nm from the wall. Notably, good agreement between experimental and calculated data is found. The full transverse EELS line-scan, performed in steps of 10 nm, is depicted in Figure 3c. Note again the enhancement of cavity modes, the pronounced shift of ω_3 , and the significant intensity difference for the bare surface plasmon at $\omega_s \approx 2.4$ eV.

The spectral dependence on slit separation (the metal bar width, d) is demonstrated in Figure 4a,b. The corresponding slit geometry is shown schematically in Figure 4c. The green (red) trajectory denotes the beam position at $L/2$, 20 nm away from the outer (inner) wall. Notably, the spectra in Figure 4a, recorded near the outer wall (green trajectory in Figure 4c), are not affected much by the distance between neighboring slits and, in fact, are all rather similar to the single-slit spectrum (green curve in Figure 4a). In contrast, marked spectral differences appear in Figure 4b for beam positions near the inner wall (red trajectory in Figure 4c). At first glance, coupling across the metal strip seems to monotonically decay with increasing d . A closer inspection reveals, however, non-monotonic interference-like features: The third multiple signal of the $d = 720$ nm sample (black spectrum), at $\omega_3 \approx 1.5$ eV, is “surprisingly” stronger than (1) ω_1 in the same spectrum and (2) ω_3 of the $d = 270$ nm sample (red spectrum). Both results correlate with the phase difference (ϕ) for SPPs propagating

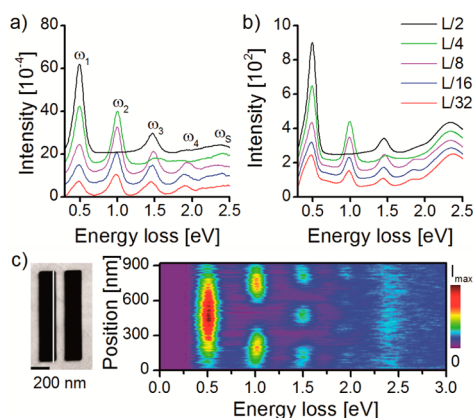


Figure 2. Scans along the slit: (a) Experimental and (b) simulated EEL spectra taken at various locations ($L/2$, $L/4$, $L/8$, $L/16$, and $L/32$) along the long slit axis at 20 nm distance from the inner wall of a two-slit system with $d = 100$ nm; (c) a color-coded EELS line-scan (right) and its corresponding HAADF STEM image (left; the white line indicates the scan).

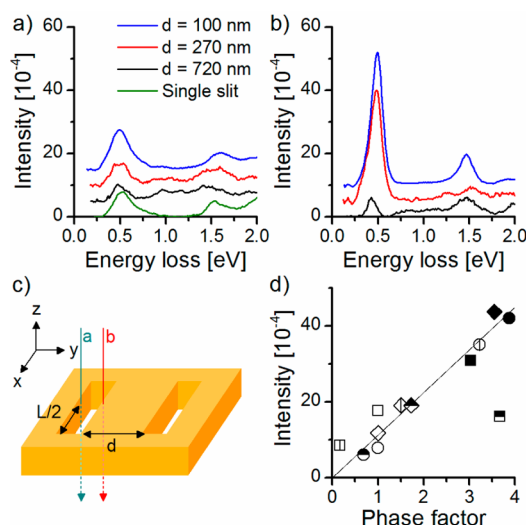


Figure 4. The effect of metal bar width, d , in the two-slit system, as visualized by EEL spectra recorded at a fixed, 20 nm distance from (a) the outer and (b) the inner wall. A corresponding schematic of the measurement position and the slit geometry is shown in (c). Green and red trajectories show the positions where spectra were taken, at the center of the long slit axis. (d) The experimental signal intensities in (b) plotted as a function of the interference phase factor, $2C_n(1 + \cos(\phi_n))$ (see text), with C_n values of 1, 1.75, and 3.5 for $n = 1, 2$, and 3, respectively. Metal bar widths of 100 nm (full symbols), 270 nm (symbols with a vertical line), and 720 nm (partially black and white symbols) are shown. The single slit is depicted by empty symbols.

across the separating metal strip, which is given by $2\pi d/\lambda$, where $\lambda = 2L/n$ is the corresponding wavelength of the n th cavity multiple.

Moreover, in contrast to the common expectation for *mode splitting* or *broadening* under coupling of two degenerate modes, the spectra from the inner wall (see Figure 4a,b) exhibit significant line *narrowing* ($\geq 30\%$), an observation further supported by large peak height enhancements (>4 , namely, above the theoretical limit for two identical modes; see SI). Previous reports on subradiant SPPs (long-living SPPs due to reduced coupling to FF decay channels) that are correlated as well with amplitude enhancements on inner metal strips^{10,11} are in general agreement with our results (albeit for different systems). Note that the line-narrowing effect, similar to the d -dependent intensity variations, does not occur for beam positions near the outer wall.

A helpful presentation of the measured line intensities is provided in Figure 4d. The figure depicts experimentally derived intensities of the ω_n multiples as a function of a phase factor, which is the square modulus of an interference amplitude, $(c_n)^{1/2}(1 + e^{i\phi_n})$, yielding $2C_n(1 + \cos(\phi_n))$, an Ansatz which will be justified below. Three sets of four data points are shown, presenting line intensities of the three major signals, ω_1 , ω_2 , and ω_3 , at the four different samples in Figure 4c. Different ω_n modes are indicated by circles, diamonds, and squares, while their filling denotes the corresponding d value. ω_2 intensities are extracted from measurements at the $L/4$ point, and wavelengths are determined by $2L/n$. A common factor, C_n , is applied to each set, accounting for the inherently different oscillator strengths of the three ω_n modes. The figure manifests a reasonably close proportionality of a variety of data points to the above phase factor, ranging between constructive (phase factors close to 4) and destructive (phase factors close

to 0) interference. A significant deviation arises only for ω_3 ($\lambda = 600$ nm) at the $d = 720$ nm case (namely, $d > \lambda$), which may indicate the limits of validity of this phenomenological description.²⁸

To justify the above description of the two-slit system, consider first the simplified case of two dominant, strongly coupled SPP modes, located around the two inner walls (outer walls neglected!). We label these modes as $|1,0\rangle$ and $|0,1\rangle$ for right- and left-hand-side localized SPPs, respectively. A general symmetry-based argument should hold here, independent of the wall-separation distance, d . Under coupling, a symmetric (S), $|1,1\rangle$, and an antisymmetric (AS), $|1,-1\rangle$, eigen-modes would emerge. The presence of odd and even mode symmetry in a similar two-slit system was previously visualized by EFTEM,¹⁹ where both slits were simultaneously illuminated. The situation in the present experiments is profoundly different because the focused electron beam couples selectively to a single wall of one particular slit (a fact verified directly from the sharp tails near each wall; see Figure 1).

A priori, no particular preference of a specific symmetry as of the coupling to an electron beam is expected, hence both S and AS modes should be excited in all samples. However, the experiment does show a clear difference in this respect: for each sample in Figure 4, a specific combination of S and AS modes is selected, depending on the phase factor in Figure 4d. We attribute this fact to the direct manifestation of SPP evolution in the time domain, initiated by the highly confined beam electron: A $|1,0\rangle$ state is dictated at $t = 0$, and its evolution with time, carried by the SPP^{Top} and SPP^{Bot} couplers, leads to a relative phase between the neighboring edges ($\phi = 2\pi d/\lambda$), namely, to the emergence of a $|1, e^{i\phi}\rangle$ mode. Obviously, at the limiting case of a single slit, corresponding to $d \rightarrow \infty$, a pure $|1,0\rangle$ mode is retained. The corresponding measured low intensity verifies that direct contributions of SPP^{Top/Bot} to the loss function are rather small. In contrast, at the $d \rightarrow 0$ limit the two inner walls are excited in-phase. Hence, one expects at the $d \rightarrow 0$ limit, with doubled state amplitude, a 4-times larger signal intensity, as indeed approached for ω_1 . It is noted that the quadratic dependence on interference amplitude, $|1 + e^{i\phi}|^2$, agrees with the well-known dependence of the loss function on collective mode excitation amplitudes, for a beam-electron at resonant frequencies with the excited modes.²⁹

It is important to note that for a beam current of 1 nA, an upper limit in these experiments, only one electron is present on average in the microscope column within a time interval of ~ 100 ps. This sets an estimated time scale for the rate of sequencing scattering events. Other relevant time scales are the oscillation period of the multiples, about 6 fs for ω_1 , and the effective time of interaction between the electron and the metal film (estimated from the spatial extent of SPPs to be less than 20 fs, see SI). Considering these time scales, only a small number of oscillations are probed by each beam electron, and importantly, the system can achieve full relaxation between the ultrashort electron pulses. Consequently, insight into the femtosecond-scale, subperiod dynamics of SPP excitations is gained through our measurements. This constitutes a novel feature facilitated by STEM-EELS. In particular, ω_1 in Figure 4b demonstrates the crossover between nearly pure S and AS modes, as dictated by the early stage wave propagation from one wall to the other. Accordingly, a systematic shift (up to ~ 60 meV) is seen in the ω_1 peak energy of the three samples in Figure 4b, in agreement with Figure 3a and b and with the corresponding optical shift in ref 10. Note that the limited time

of effective interaction between the beam electron and the metal introduces uncertainty in the frequency domain, which allows mixing between these S and AS modes.

Further insight into the time evolution of SPPs and an explanation for the Ansatz regarding the phase factor for nonmonotonous coupling between neighboring slits can be gained from the computed field maps. A movie depicting the evolution of the electrical field with time is given in the SI. Assuming that at long times the eigen-modes become more pronounced, one can identify, for instance, the ~ 0.5 eV signal as an ~ 8 fs oscillation in Figure 5. As expected, the transverse

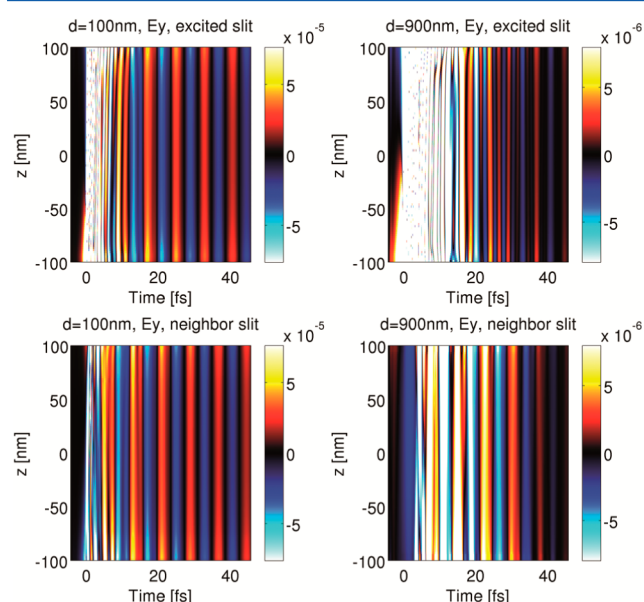


Figure 5. Color-coded simulated E_y field component parallel to the Au film, plotted as a function of time and vertical axis, z , parallel to the electron beam, in the two-slit system (axes are the same as in Figure 4c). The computations correspond to electron trajectories similar to the red trajectory (inner wall) in Figure 4c for $d = 100$ nm (left) and $d = 900$ nm (right), as induced in the excited slit (top) and the neighboring slit (bottom). Note specifically the long lasting oscillations at a period of ~ 8 fs, corresponding to the fundamental mode at ~ 0.5 eV.

field component, E_y (which is parallel to the gold film), appears at comparable intensities in both slits (near their inner walls; left panels in Figure 5), however, with a substantial delay in initial rise-up when the distance between the slits is increased (right panels in Figure 5). Interestingly, for $d = 100$ nm, E_y is roughly at antiphase between the two slits and nearly in-phase for $d = 900$ nm. In contrast, the longitudinal component, E_z , also represented by the calculated spectra in Figures 2 and 3, appears in-phase for $d = 100$ nm and at antiphase for $d = 900$ nm (for additional details, see SI at the limit of long times).

In spite of model assumptions that tend to overemphasize specific scattering components, Figure 5 points reliably to an important aspect of the interslit coupling mechanism: E_z roughly follows the phase factor in Figure 4d, and since it is the dominant component in the loss function, the EELS data are described successfully within the above simplified frame. In contrast, E_y is phase-shifted at the neighboring slit by $\sim \pi$, compared to E_z and, thus, presents AS characteristics for $d = 100$ nm. Being the dominant far-field EM component (for light propagation perpendicular to the film face), E_y induces in its AS state reduced FF amplitudes. Two important consequences

emerge here: (1) the EELS (NF) bright mode corresponds to an optically (FF) dark mode and vice versa; (2) the SPP FF decay channels are highly suppressed under small- ϕ interslit coupling, a fact giving rise to enhanced lifetimes and, hence, to significant line narrowing, as experimentally manifested by Figures 2–4.

Of particular simplicity, the SI movies (see the $d = 100$ nm example at long times) demonstrate the emergence of a *breathing mode* for $d \ll \lambda$: The field around the four faces of the metal strip undergoes collective outward–inward oscillations; i.e., a phase difference of π appears between both walls and between the two opposing (top and bottom) film faces. Then, essentially, a single field component only (normal to the surface) remains on each wall/face, and the E_z tails that extend above and below the film in the z -direction gain a dominant role.

As already hinted above, our results exhibit considerable similarity with the time-resolved optical measurements by Ropers et al.,¹⁰ where (1) S and AS modes could be spatially and energetically differentiated and (2) line narrowing appeared together with reduced radiative SPP decay. On the other hand, major spectroscopic features of the STEM-EELS are unique. First, the *femtosecond-time-scale dynamics* triggered by the electron passage across a nanocavity (see the SI movies) is by far richer than the optically triggered dynamics. Second, in contrast to optical techniques, the electron beam (also in EFTEM) is exclusively sensitive to the E_z field component. Therefore, combined with its superior lateral resolution, the beam presents a novel capability to locally probe *hot spots* (e.g., slit rims and edges) where enhanced *coupling between radiative and nonradiative* field components takes place, a topic of great importance in plasmonics. Third, the inspection of *film-supported* nonlocal processes, such as SPP interference, can be achieved with practically all dominant (longitudinal) *beam-related* field components eliminated, a feature missing from all broad beam techniques including EFTEM. Additional complementary aspects of the time-dependent findings probed by our focused electron beam vs the broad-beam works may be noted: (1) Ropers et al. explore top–bottom SPP coupling and not the laterally interacting walls. (2) Their large hole arrays consist of well-defined lattice resonances, in contrast to our samples. Altogether, insight is gained here on the physics at the single-slit level and its sensitivity to neighboring patterns that is not quite available by optical means.

As a final remark, generalization of the phenomenological phase-factor approach to account for the full array is rather straightforward. We assume a 1D set of localized modes, subject to nearest-neighbors' interactions, with two complex parameters, γ_1 and γ_2 , that represent, respectively, the intra- and interslit coupling. The signal intensity at a given location is obtained then by summing over contributions from all the array modes, as described in detail in the SI. Two major results arise from this phenomenological model: (1) For $d = 100$ nm we obtain $|\gamma_1| = 0.083$ and $|\gamma_2| = 0.95$, which indicates an order of magnitude difference between inter- and intraslit coupling.³⁰ (2) We find indeed an initial striking signal increase as a function of the slit number N , but it is followed by a slight signal *decrease* for sufficiently long arrays. Experimental hints for the latter result have been observed, for example, in the slight intensity decrease at the center of the eight-slit system (cf. Figure 1d). These effects present additional fingerprints of the intriguing, coherent dielectric response realized in the coupled-slits system.

CONCLUSIONS

In summary, using a focused electron beam we have explored cavity resonances in 1D slit arrays. Short-range interactions between highly confined SPP modes are found to dominate the EM activity of the patterned gold film and, already in the case of two slits only, give rise to remarkable signal enhancements and line narrowing. In turn, this provides spectral fingerprints of the transient signal propagation from one slit edge to the other, corresponding to a retarded and thus distance-dependent interaction. The emerging physical picture of ultrafast, coherent dielectric response is strongly supported by exact real space–time numerical simulations, revealing the origin of increased SPP lifetimes for in-phase oscillations. The introduction of femtosecond-scale *time dependencies* to the EELS interpretation opens a novel dimension of applications. We have specifically demonstrated the rich dynamics induced by the beam electron around hot spots like the slit edges, as well as the development of a high-symmetry breathing mode and its distortion upon increased interslit distances. Besides its superior spatial resolution, the highly focused electron beam, combined with DGT simulations, thus offers unique capabilities for ultrafast subwavelength electrodynamics studies in general and the EOT mechanisms in particular.

ASSOCIATED CONTENT

Supporting Information

Numerically simulated E_z -field components including movies and phenomenological model of next-neighbor coupling. This material is available free of charge via the Internet at <http://pubs.acs.org>.

AUTHOR INFORMATION

Corresponding Authors

*E-mail: hagai.cohen@weizmann.ac.il.

*E-mail: itai@post.tau.ac.il.

Author Contributions

• R.W. and I.C. contributed equally

Notes

The authors declare no competing financial interest.

ACKNOWLEDGMENTS

This research was supported by a cooperation grant of the Karlsruhe Institute of Technology's Center for Functional Nanostructures (CFN), the Weizmann Institute nano initiative (WINI), and the Technion Russell Berrie nanotechnology institute (RBNI) and by the Weizmann's Helen and Martin Kimmel Center for Nanoscale Science (HC) and Infrastructures fund (SR). K.B. and C.M. acknowledge support by the Deutsche Forschungsgemeinschaft (DFG) through project Bu 1107/7-2.

REFERENCES

- (1) Ebbesen, T. W.; Lezec, H. J.; Ghaemi, H. F.; Thio, T.; Wolff, P. A. Extraordinary Optical Transmission through Sub-Wavelength Hole Arrays. *Nature* **1998**, *391*, 667–669.
- (2) Coe, J. V.; Heer, J. M.; Teeters-Kennedy, S.; Tian, H.; Rodriguez, K. R. Extraordinary Transmission of Metal Films with Arrays of Subwavelength Holes. *Annu. Rev. Phys. Chem.* **2008**, *59*, 179–202.
- (3) Vengurlekar, A. S. Extraordinary Optical Transmission through Metal Films with Subwavelength Holes and Slits. *Curr. Sci. India* **2010**, *98*, 1020–1032.

- (4) Garcia-Vidal, F. J.; Martin-Moreno, L.; Ebbesen, T. W.; Kuipers, L. Light Passing through Subwavelength Apertures. *Rev. Mod. Phys.* **2010**, *82*, 729–787.
- (5) Genet, C.; Ebbesen, T. W. Light in Tiny Holes. *Nature* **2007**, *445*, 39–46.
- (6) Garcia de Abajo, F. J. Optical Excitations in Electron Microscopy. *Rev. Mod. Phys.* **2010**, *82*, 209–275.
- (7) Maier, S. A. *Plasmonics: Fundamentals and Applications*; Springer Science LLC: New York, 2007.
- (8) Pacifici, D.; Lezec, H. J.; Atwater, H. A.; Weiner, J. Quantitative Determination of Optical Transmission through Subwavelength Slit Arrays in Ag Films: Role of Surface Wave Interference and Local Coupling between Adjacent Slits. *Phys. Rev. B* **2008**, *77*, 115411–5.
- (9) Fernandez-Dominguez, A. I.; Garcia-Vidal, F. J.; Martin-Moreno, L. Resonant Transmission of Light through Finite Arrays of Slits. *Phys. Rev. B* **2007**, *76*, 235430–7.
- (10) Ropers, C.; Park, D. J.; Stibenz, G.; Steinmeyer, G.; Kim, J.; Kim, D. S.; Lienau, C. Femtosecond Light Transmission and Subradiant Damping in Plasmonic Crystals. *Phys. Rev. Lett.* **2005**, *94*, 113901–4.
- (11) Kim, D. S.; Hohng, S. C.; Malyarchuk, V.; Yoon, Y. C.; Ahn, Y. H.; Yee, K. J.; Park, J. W.; Kim, J.; Park, Q. H.; Lienau, C. Microscopic Origin of Surface-Plasmon Radiation in Plasmonic Band-Gap Nanostructures. *Phys. Rev. Lett.* **2003**, *91*, 143901–4.
- (12) Bouillard, J. S.; Vilain, S.; Dickson, W.; Zayats, A. V. Hyperspectral Imaging with Scanning near-Field Optical Microscopy: Applications in Plasmonics. *Opt. Express* **2010**, *18*, 16513–16519.
- (13) Gao, H. W.; Henzie, J.; Odom, T. W. Direct Evidence for Surface Plasmon-Mediated Enhanced Light Transmission through Metallic Nanohole Arrays. *Nano Lett.* **2006**, *6*, 2104–2108.
- (14) von Cube, F.; Irsen, S.; Diehl, R.; Niegemann, J.; Busch, K.; Linden, S. From Isolated Metaatoms to Photonic Metamaterials: Evolution of the Plasmonic near-Field. *Nano Lett.* **2013**, *13*, 703–708.
- (15) Rossouw, D.; Botton, G. A. Plasmonic Response of Bent Silver Nanowires for Nanophotonic Subwavelength Waveguiding. *Phys. Rev. Lett.* **2013**, *110*, 066801–5.
- (16) Carmeli, I.; Itskovsky, M. A.; Kauffmann, Y.; Shaked, Y.; Richter, S.; Maniv, T.; Cohen, H. Far- and near-Field Electron Beam Detection of Hybrid Cavity-Plasmonic Modes in Gold Microholes. *Phys. Rev. B* **2012**, *85*, 041405–5.
- (17) Cohen, H.; Maniv, T.; Tenne, R.; Hacohen, Y. R.; Stephan, O.; Colliex, C. Near-Field Electron Energy Loss Spectroscopy of Nanoparticles. *Phys. Rev. Lett.* **1998**, *80*, 782–785.
- (18) Itskovsky, M. A.; Cohen, H.; Maniv, T. Radiative Interaction of a Focused Relativistic Electron Beam in Energy-Loss Spectroscopy of Nanoscopic Platelets. *Phys. Rev. B* **2008**, *78*, 045419–11.
- (19) Ögüt, B.; Vogelgesang, R.; Sigle, W.; Talebi, N.; Koch, C. T.; van Aken, P. A. Hybridized Metal Slit Eigenmodes as an Illustration of Babinet's Principle. *ACS Nano* **2011**, *5*, 6701–6706.
- (20) Schaffer, B.; Hohenester, U.; Trugler, A.; Hofer, F. High-Resolution Surface Plasmon Imaging of Gold Nanoparticles by Energy-Filtered Transmission Electron Microscopy. *Phys. Rev. B* **2009**, *79*, 041401–4.
- (21) Matyssek, C.; Niegemann, J.; Hergert, W.; Busch, K. Computing Electron Energy Loss Spectra with the Discontinuous Galerkin Time-Domain Method. *Photonics Nanostruct.* **2011**, *9*, 367–373.
- (22) Busch, K.; König, M.; Niegemann, J. Discontinuous Galerkin Methods in Nanophotonics. *Laser Photonics Rev.* **2011**, *5*, 773–809.
- (23) Bosman, M.; Keast, V. J. Optimizing EELS Acquisition. *Ultramicroscopy* **2008**, *108*, 837–846.
- (24) Zuo, J. M. Electron Detection Characteristics of a Slow-Scan CCD Camera, Imaging Plates and Film, and Electron Image Restoration. *Microsc. Res. Technol.* **2000**, *49*, 245–268.
- (25) Gloter, A.; Douiri, A.; Tence, M.; Colliex, C. Improving Energy Resolution of EELS Spectra: An Alternative to the Monochromator Solution. *Ultramicroscopy* **2003**, *96*, 385–400.
- (26) Al-Bakkar, A. G.; Ipson, S. S.; Porter, G. J.; Gleed, D. G. A Parallel Implementation of a Modified Richardson-Lucy Algorithm for

Image De-Blurring. *Int. J. Infrared Millimeter Waves* **1997**, *18*, 555–575.

(27) Johnson, P. B.; Christy, R. W. Optical Constants of Noble Metals. *Phys. Rev. B* **1972**, *6*, 4370–4379.

(28) It is stressed that the nominal wavelengths, $\lambda = 2L/n$, are the ones applied successfully to this phenomenological description. Further study of the actual SPP dispersion and of the physical origin of this fact will be given in the future.

(29) Sunjic, M.; Lucas, A. A. Multiple Plasmon Effects in Energy-Loss Spectra of Electrons in Thin Films. *Phys. Rev. B* **1971**, *3*, 719–729.

(30) Coupling strength to the next slit edge a few percent of the major term is estimated for an electron beam positioned 20 nm from a given wall. It is applied as a mixing parameter in the simulations (see Supporting Information).